Atomic alignment of $_{73}$Ta, $_{74}$W, and $_{79}$Au after L_3 subshell ionization by 10–100-keV electron impact

Suelen F. Barros*
Instituto Federal de São Paulo, Rua Primeiro de Maio 500, Bairro Estação, CEP:08571-050 Itaquaquecetuba, SP, Brazil and Instituto de Física, Universidade de São Paulo, Rua do Matão 1371, Cidade Universitária, CEP:05508-090 São Paulo, SP, Brazil

Vito R. Vanin, Alessio Mangiarotti, and Nora L. Maidana
Instituto de Física, Universidade de São Paulo, Rua do Matão 1371, Cidade Universitária, CEP:05508-090 São Paulo, SP, Brazil

José M. Fernández-Varea
Facultat de Física (FQA and ICC), Universitat de Barcelona, Diagonal 645, ES-08028 Barcelona, Catalonia, Spain and Instituto de Física, Universidade de São Paulo, Rua do Matão 1371, Cidade Universitária, CEP:05508-090 São Paulo, SP, Brazil

(Received 4 October 2019; published 10 December 2019)

The alignment parameter A_{20} of $_{73}$Ta, $_{74}$W, and $_{79}$Au ions after L_3 subshell ionization by electron impact has been determined experimentally and theoretically in the wide energy range $(1.02–10.2)E_{L_3}$, where E_{L_3} is the L_3 ionization threshold. The A_{20} values have been deduced from measurements of the $L\ell$ ($L_3 \to M_1$), $L\alpha_2$ ($L_3 \to M_4$), and $L\alpha_1$ ($L_3 \to M_5$) x-ray angular distributions using thin targets. The beam energies have been selected above the threshold energy of each L subshell in order to also investigate the influence of the Coster-Kronig transitions on the anisotropy of x-ray emission. The results provide a clear indication of alignment and agree with calculations carried out within the plane-wave Born approximation up to about $6E_{L_3}$, but an unpredicted inversion in the sign of A_{20} is observed above this energy.

DOI: 10.1103/PhysRevA.100.062705

I. INTRODUCTION

As noted by Bohr in his Nobel Prize speech, the atom is a quantal system that does not rotate collectively [1]. Therefore, it may be surprising to learn that excitation or ionization by electron impact can align the angular momentum despite the spherical symmetry of the initial wave function of the target. As a matter of fact, it is by now well known that electron impact on *outer* atomic shells can align and orient the atom when the *excited* electron comes from a state with total angular momentum $j \geqslant \frac{3}{2}$ [2], resulting in the subsequent emission of fluorescent radiation with a nonisotropic angular distribution. Electron impact can also *ionize* the atom. Again, in circumstances in which the ejected electron comes from a state with $j \geqslant \frac{3}{2}$ it is expected on purely theoretical grounds that the emitted fluorescent radiation is not isotropic [3]. While the alignment and orientation of external atomic subshells in the excitation by electron impact is a thoroughly studied phenomenon [2], in the case of electron-impact ionization it had not been observed conclusively.

The magnitude of the alignment when an unpolarized beam of charged particles ionizes an atomic subshell is quantified by the parameter A_{20} which, for the L_3 subshell ($j = \frac{3}{2}$), is calculated as the relative difference of the ionization cross sections $\sigma(j, m_j)$ pertaining to the states with $m_j = \frac{3}{2}$ and $m_j = \frac{1}{2}$,

$$A_{20} = \frac{\sigma\left(\frac{3}{2}, \frac{3}{2}\right) - \sigma\left(\frac{3}{2}, \frac{1}{2}\right)}{\sigma\left(\frac{3}{2}, \frac{3}{2}\right) + \sigma\left(\frac{3}{2}, \frac{1}{2}\right)}. \tag{1}$$

When the only direction defined by the experimental conditions is that of the unpolarized incident beam, the ionization cross sections of an inner-shell electron with quantum numbers n, ℓ, j, m_j in Eq. (1) are independent of the sign of m_j. Then $\sigma(\frac{3}{2}, \frac{3}{2}) \neq \sigma(\frac{3}{2}, \frac{1}{2})$ while $\sigma(\frac{3}{2}, \frac{3}{2}) = \sigma(\frac{3}{2}, -\frac{3}{2})$ and $\sigma(\frac{3}{2}, \frac{1}{2}) = \sigma(\frac{3}{2}, -\frac{1}{2})$, A_{20} will be nonzero and the system is classified as aligned, but not oriented. When also the ionization cross sections of states m_j and $-m_j$ are different, the system is said to be oriented [3].

On the other hand, A_{20} can be established experimentally from the angular distribution of Auger electrons or characteristic x rays as well as from the polarization of the radiation emitted in the subsequent decay of singly ionized atoms. Previous experiments on the alignment by electron impact [4–14] could not determine the energy dependence and even the scale of the phenomenon. Experiments that relied on Auger electron spectroscopy [4–9] were limited to low-Z elements. The measured A_{20} values have large uncertainties because the postcollision Coulomb interaction among the three emerging electrons changes the shape of the peaks in the energy spectrum and attenuates the angular distribution [7,8], especially near the ionization threshold. Moreover, electron-electron correlation in elements with low Z blur the systematic behavior we unveil in this work with higher-Z elements. Figure 1 presents the alignment parameters measured from the angular distribution or the polarization of the emitted

*suelen.barros@ifsp.edu.br; suelenb@if.usp.br

 ©2019 American Physical Society

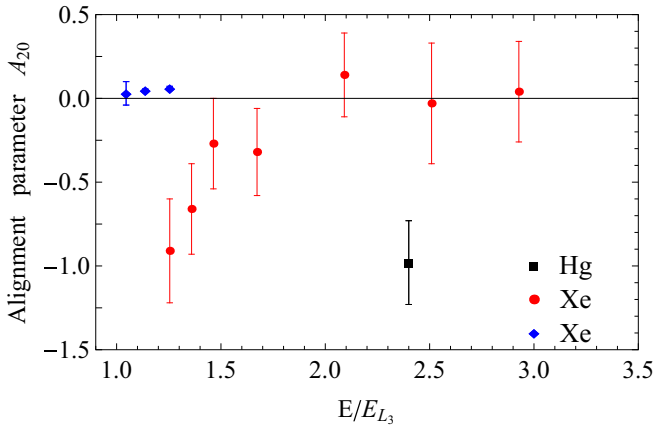

FIG. 1. Previous measurements of the alignment parameter A_{20} after electron-impact ionization as a function of E/E_{L_3} for $Z \gtrsim 50$. ■, $_{80}$Hg [10]; ●, $_{54}$Xe [12]; ♦, $_{54}$Xe [13].

characteristic radiation, for elements with $Z \gtrsim 50$ [10,12,13], as a function of E/E_{L_3}, where E is the incident electron beam energy and E_{L_3} is the ionization energy of the L_3 subshell. References [11,14] have found an isotropic emission within the experimental uncertainties for the investigated L lines, but they did not report estimates for A_{20}. The degree of polarization P of the Xe $L\alpha$ doublet measured by Aydinol *et al.* [12] has been transformed into the alignment parameter A_{20} using Eq. (18) in Ref. [3]. These few data highlight that the existing measurements by electron impact prior to this work are discrepant, do not allow one to determine the magnitude of the alignment parameter of the ions, and fail even in proving that L x-ray emission is anisotropic.

The results of measurements done by photoionization cannot be compared with each other directly because they were performed with different elements, energies, and photon-beam polarization degrees [15–22]. The results of the few experiments that were carried out under the same conditions are not consistent with each other [15–19], as highlighted by Santra *et al.* [21].

The related phenomenon of alignment by the impact of swift positive ions (protons, alpha particles, ...) is better known. The trend of the experimental data is similar to the calculated values [23–26]. However, they do not extend to energies where the ejected electron is relativistic.

There has been extensive research on total cross sections for L-subshell ionization by electron impact, most often determined from the yield of the emitted characteristic x rays. The total cross section is an average over the magnetic states and thus insensitive to the projection of the angular momentum of the ionized atom. This averaging procedure cannot be used to explain the atomic alignment, and therefore the alignment measurement uncovers new information and furnishes an important and effective testing ground for theoretical models of the ionization process. Incidentally, the current measurements of ionization cross sections do not take into account the angular distribution of the characteristic radiation [27,28], leading to systematic errors, which we will evaluate and show that they are small except in special circumstances.

TABLE I. Energies of the L subshell thresholds and the $L\ell$, $L\alpha_2$, and $L\alpha_1$ characteristic x rays, in keV, for $_{73}$Ta, $_{74}$W, and $_{79}$Au [29].

		Energy (keV)		
		$_{73}$Ta	$_{74}$W	$_{79}$Au
Subshell	L_1	11.6821(16)	12.09973(87)	14.35529(50)
	L_2	11.1329(14)	11.5386(16)	13.734194(70)
	L_3	9.8767(12)	10.2001(12)	11.919694(60)
Transition	$L\ell$	7.17320(31)	7.38782(65)	8.49403(78)
	$L\alpha_2$	8.08793(16)	8.33534(17)	9.62805(33)
	$L\alpha_1$	8.14617(16)	8.398242(54)	9.71344(34)

In the experiment described here, the difficulties encountered in older investigations have been overcome by an improved setup and data-analysis method. We have measured the alignment parameter A_{20} for $_{73}$Ta, $_{74}$W, and $_{79}$Au ions with a vacancy in the L_3 subshell generated by electron impact in the wide energy interval $(1.02–10.2)E_{L_3}$, approximately (10–100) keV. This parameter is estimated from the angular distributions of the transitions of L_3 vacancies to subshells M_1, M_4, and M_5, denoted, respectively, as $L\ell$, $L\alpha_2$, and $L\alpha_1$, whose energies are given in Table I. Our measurements offer an answer to the existence of atomic alignment in the ionization by electron impact, and disclose the dependence of this alignment with the electron energy. The available theoretical model [3], although successful near the ionization threshold, is unable to explain the observed behavior at energies $\gtrsim 6E_{L_3}$.

The paper is structured as follows. The experimental method and subsequent data-analysis procedure are explained in Secs. II and III, respectively. The theory is outlined in Sec. IV. Section V presents the measured and calculated alignment parameters and Sec. VI discusses the results. Our conclusions are summarized in Sec. VII.

II. EXPERIMENT

The alignment of $_{73}$Ta, $_{74}$W, and $_{79}$Au atoms has been measured in the (10–100)-keV beam line of the São Paulo Microtron [30], using a $_{29}$Cu target to monitor the efficiency of the x-ray spectrometers at each energy, and $_{29}$Cu and $_{46}$Pd targets to determine the *relative* efficiencies of the three detectors employed. When relevant for the present experiment, we include a concise description of the setup, which is similar to those used in earlier measurements of cross sections for bremsstrahlung emission and for the ionization of K and L (sub)shells (see Refs. [31–33]), and it is discussed in detail in Ref. [30].

A. Preparation and characterization of the targets

The targets of $_{29}$Cu, $_{73}$Ta, and $_{74}$W have been manufactured by sputtering from a metallic disk, and the $_{46}$Pd and $_{79}$Au targets by physical vapor deposition through a mask that limited the target surface area to a circle 8 mm in diameter, in both techniques. These elements have been deposited on $_{6}$C backings with thicknesses of the order of 50 nm, held by frames also made of $_{6}$C with dimensions of $15 \times 30 \times 0.3$ mm^3, and a central circular hole 10 mm in diameter.

The areal densities $\mathcal{N}d$ ($\mathcal{N}$ is the number of atoms per unit volume and d is the film thickness) of the Cu/C, Pd/C, Ta/C, W/C, and Au/C films have been measured by Rutherford backscattering spectrometry with 2200(11) keV $^4He^+$ ions at the LAMFI Pelletron tandem accelerator [34]. The targets have been placed in the center of the irradiation chamber, tilted 7° with respect to the incident beam direction. The energy spectra of the backscattered ions have been acquired with a surface barrier Si detector, positioned at 120° with respect to the incident beam direction, and analyzed with the MULTISIMNRA code [34]. Typical backscattering spectra of the three targets employed in the measurement of x-ray angular distributions, and of the Cu/C target used as monitor, are presented in Fig. 2, together with the simulated spectra for the profiles fitted by MULTISIMNRA.

In order to quantify the target uniformity, some targets have been irradiated with the $^4He^+$ beam at more than one spot. The Ta/C and Au/C targets have been irradiated in the center, above, and below it, and the Cu/C target in the center, below, above, to the left, and to the right of it. The displacements are of the order of 3 mm, somewhat larger than the 2 mm diameter of the ion beam. The standard deviations of these mass thicknesses in different points are 0.5, 0.5, and 0.3 $\mu g/cm^2$ for the Cu/C, Ta/C, and Au/C targets, respectively. The standard deviation associated with the areal densities of the targets have been obtained adding quadratically these estimates of the nonuniformity with the standard deviations resulting from the fit with the MULTISIMNRA software.

The areal densities of the Cu, Pd, Ta, W, and Au films and their uncertainties (one standard deviation) are, respectively, 160(6), 142(8), 55(3), 12.5(9), and 30.9(9) in units of 10^{15} atoms/cm^2. These values correspond to mass thicknesses equal to 16.9(6), 24.6(14), 16.5(9), 3.8(3), and 10.1(3) $\mu g/cm^2$, respectively.

B. Irradiation chamber and Faraday cup

The chamber used in the experiment has a cylindrical steel wall, with internal and external diameters of 490 and 500 mm, respectively. The chamber is designed to measure x-ray angular distributions; to this end it has 13 flanges distributed between the angles of 31° and 166° relative to the electron beam direction, chosen close to the zeros and extremes of the Legendre polynomials of orders two and four. The chamber lid is made of Al and it holds the movable target ladder for up to six targets plus a BeO view screen to monitor the beam location and profile. The spectroscopy windows of the chamber are made of Al and Kapton, with thicknesses of 5 and 25 μm, respectively. In this experiment, the internal part of the flanges is equipped with Al cylindrical collimators, 9 mm in diameter and 70 mm in length, installed to narrow the area of the chamber internal wall that is visible to the detectors without reducing their active area.

A conical Faraday cup made of graphite, with a half-aperture angle of 12° and 200 mm deep, is coupled to the chamber at 0° with respect to the incident beam direction. Monte Carlo simulations have shown that this design reduces the probability of electron backscattering and the production of photons [30]. Both the Faraday cup and the chamber are electrically insulated, and the collected charges have been measured separately using current integrators. Their sum gives the total charge incident on the target during each irradiation, and their ratio is used to evaluate the amount of elastic scattering of the electrons in the target, which attenuates the x-ray angular distribution.

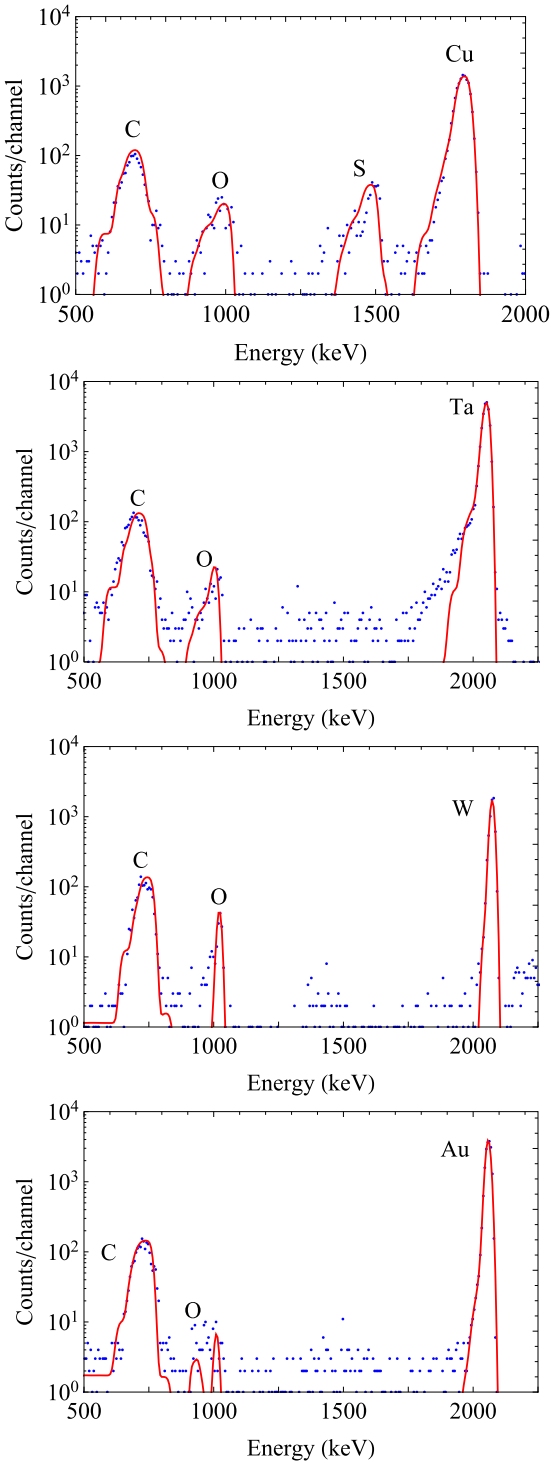

FIG. 2. Rutherford backscattering spectra of 2200(11) keV $^4He^+$ ions incident on the (a) Cu/C, (b) Ta/C, (c) W/C, and (d) Au/C targets. The dots are the experimental values and the curves are the MULTISIMNRA simulated spectra. The energy dispersion is approximately 6.5 keV/channel for the Cu/C target and 6 keV/channel in the other cases.

C. X-ray spectrometers

Unlike the experiments done so far [10–14], the x-ray yields at different angles have been measured *simultaneously* using three Si drift detectors (SDD; Amptek, Bedford, USA). Each spectrometer has a 0.5-mm-thick Si crystal with a 25 mm^2 front face, covered by an internal collimator with an area of 17 mm^2 (nominal values). The 12.7-μm-thick Be window is separated by 1.4 mm from the front surface of the active volume. The detectors have been placed at 31.1(5)°, 90.2(5)°, and 125.0(5)° with respect to the beam direction, outside the vacuum chamber, 12.5(5) mm away from the spectroscopy windows and 315(2) mm from the target. The digital spectrometers have two analyzing channels: a fast one for accurate pile-up detection and a slow one that achieves a resolution (FWHM) of 140 eV at 6.4 keV (Fe $K\alpha$ doublet). A scaler is associated with each detector to accumulate the pulses from the charge integrator during the irradiation runs, gated by the respective multichannel analyzer (MCA) enable logic signal.

The SDDs have been calibrated in energy resorting to the γ- and x-ray peaks from certified ^{57}Co, ^{133}Ba, and ^{241}Am radioactive sources.

The *relative* efficiency of the spectrometers is evaluated using the areas of the $_{29}$Cu $K\alpha_1$ and $_{46}$Pd $K\alpha_1$ peaks, which have been obtained by irradiating the Cu/C and Pd/C targets with electrons of 55, 65, 75, 85, and 100 keV, in conjunction with a full-energy peak (FEP) efficiency model whose adjustable parameters are the fraction of solid angle subtended by the detector, $\Omega/(4\pi$ sr), and the thickness $\mathcal{L}$ of the Si crystal.

As will be explained in Sec. III, the methodology to estimate the alignment parameter requires the efficiency ratio $\varepsilon_{\rm abs}(E_{K\alpha})/\varepsilon_{\rm abs}(E_i)$, where $\varepsilon_{\rm abs}$ is equal to the photon flux transmission times the intrinsic efficiency ε [35], and $E_{K\alpha}$ and E_i are the energies of the $K\alpha$ line used as reference and of the line i of interest, respectively. The only parameter that contributes to the uncertainty of these efficiency ratios is the detector crystal thickness $\mathcal{L}$ because the solid angle does not appear in this ratio. To accurately estimate the thickness $\mathcal{L}_n$ of the detector n, with its uncertainty, a procedure has been proposed which is based on an analytical model of the FEP efficiency and the areas of the $_{29}$Cu $K\alpha_1$ and $_{46}$Pd $K\alpha_1$ x-ray peaks.

First, the parameters of the FEP efficiency model, $\varepsilon_{\rm FE}(E)$, are fitted to the experimental values measured with the same certified sources employed in the energy calibration, as described in Refs. [35,36]. This model expresses $\varepsilon_{\rm FE}(E)$ as the product of three factors, namely, the geometric efficiency, the photon flux transmission, and the intrinsic efficiency of the spectrometer. Figure 3 depicts, for the three spectrometers, the experimental values and the $\varepsilon_{\rm FE}(E)$ curves calculated with the fitted parameters. The model describes adequately the FEP efficiency of the SDDs, besides making it clear that the three detectors are similar. The estimated Si crystal thicknesses deduced from these fits have uncertainties of the order of 3%. However, the anisotropy of the investigated lines is expected to be barely a few percent [3]. Hence, the thicknesses $\mathcal{L}_n$ need to be known with a better precision so that the uncertainty in the efficiency ratios $\varepsilon_{\rm abs}(E_{K\alpha})/\varepsilon_{\rm abs}(E_i)$ does not jeopardize the final precision of the x-ray angular distributions.

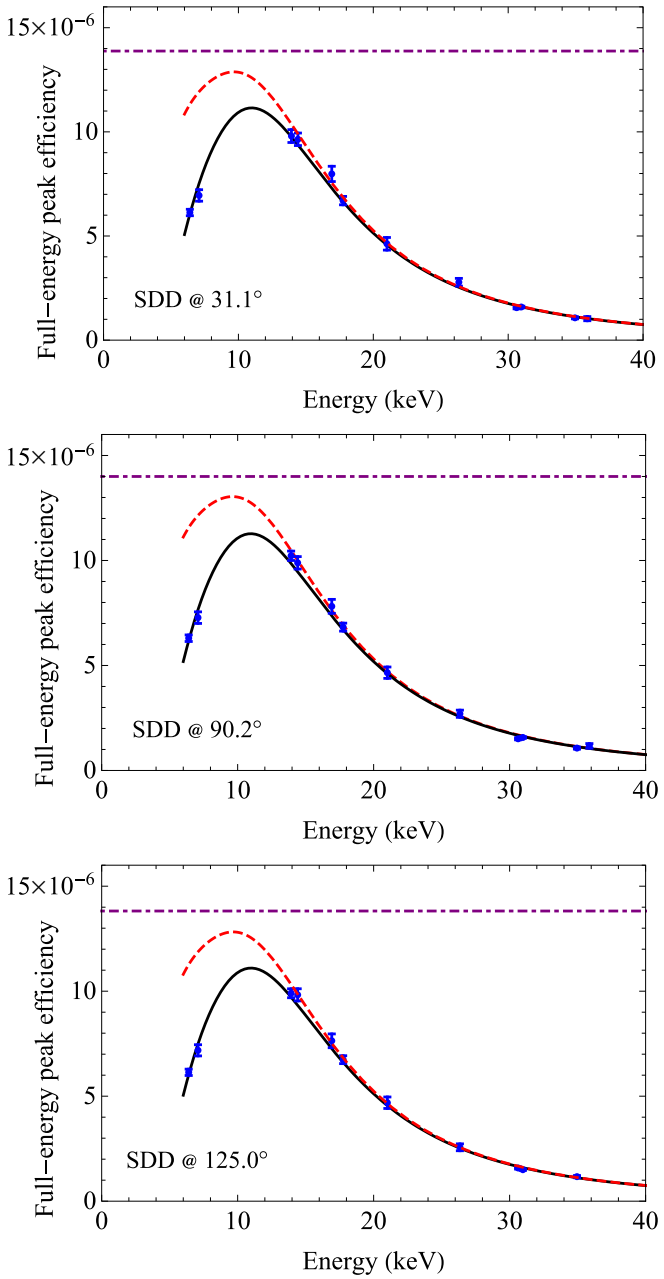

FIG. 3. FEP efficiencies of the SDDs placed at (a) $\theta_1 = 31.1°$, (b) $\theta_2 = 90.2°$, and (c) $\theta_3 = 125.0°$ with respect to the beam direction. The circles with uncertainty bars (one standard deviation) are the experimental values. The curves are the efficiencies calculated with the fitted parameters. The solid curves account for the attenuator thicknesses (air, Kapton) appropriate to the calibration with radioactive sources whereas the dashed ones pertain to the electron-beam irradiation conditions (evacuated chamber). The dot-dashed horizontal lines indicate the geometrical efficiencies, $\Omega/(4\pi$ sr).

According to the theoretical predictions [3], K x-ray emission must be isotropic (they originate from a $j = \frac{1}{2}$ vacancy), which was studied by Yamaoka *et al.* [19], and also verified experimentally here. Therefore, from the $K\alpha$ peak areas we can calculate the quotient $r^{\rm expt}_{E,n}$ that only depends on the energy E of the incident electrons and on the absolute efficiency of

TABLE II. High-precision estimates of the Si crystal thicknesses of the SDDs. The numbers in parentheses are the standard deviations in units of the least significant digit.

Detector angle	$\hat{\mathcal{L}}$ (mm)
31.1°	0.5034(3)
90.2°	0.4956(3)
125.0°	0.4885(3)

the detector,

$$r_{E,n}^{\text{expt}} = \frac{A_{\text{Pd}}}{\nu_{\text{Pd}} Q_{\text{Pd}} \tau_{\text{Pd}}} \frac{\nu_{\text{Cu}} Q_{\text{Cu}} \tau_{\text{Cu}}}{A_{\text{Cu}}}, \tag{2}$$

where the subscripts indicate the target element ($_{29}$Cu or $_{46}$Pd), A is the area of the $K\alpha_1$ peak, Q is the charge collected during the irradiation, τ is a dimensionless factor that corrects for the detector dead time, and ν is the fraction of photons transmitted through the target. Then, it is possible to write

$$r_{E,n} = \mathcal{C}(E) R_{\varepsilon_{\text{abs}}}(\mathcal{L}_n) \tag{3}$$

in which $R_{\varepsilon_{\text{abs}}}(\mathcal{L}_n) = \varepsilon_{\text{abs}}(E_{\text{Pd}}, \mathcal{L}_n)/\varepsilon_{\text{abs}}(E_{\text{Cu}}, \mathcal{L}_n)$, where E_{Cu} and E_{Pd} correspond to the Cu and Pd $K\alpha_1$ energies, respectively, and the energy-dependent factor $\mathcal{C}(E)$, which is part of the model, was not needed in the rest of the analysis. The model parameters to be fitted to the experimental data are, therefore, $\mathcal{C}(E)$ and $\mathcal{L}_n$ for each detector. The procedure adopted to fit the parameters of Eq. (3) to the experimental data of Eq. (2) is presented in the Appendix. The fitted values of the Si crystal thicknesses and their uncertainties are listed in Table II.

It is important to mention that in the proposed procedure the targets must be thin enough to guarantee that photon self-attenuation is practically the same at the angles where the detectors are positioned. The associated correction is then so small that it can be neglected and does not add uncertainty to the thickness estimates.

The curves calculated from the analytical model with the thicknesses $\mathcal{L}$ presented in Table II, and with the attenuation factors appropriate to the irradiation conditions, have been used to evaluate the relative efficiencies.

D. Measurement of x-ray spectra

The acquisition rates have ranged between 2 and 12 kHz, and the irradiations lasted from 3 to 6 h, alternating between a 1-h run with the element of interest and a 5-min run with Cu/C. More than 10^5 counts have been collected in the $L\ell$ peaks of $_{73}$Ta, $_{74}$W, and $_{79}$Au, an order of magnitude larger than that quoted in most articles on this subject that indicate this information (see Refs. [18,21]). As K x-ray emission is predicted to be isotropic [3], the $_{29}$Cu K x rays served to monitor the anisotropy of the experimental arrangement.

The energies for the irradiation of the Ta/C and Au/C targets have been chosen between the L_3 ionization threshold up to 100 keV, with some values just above the L_3 threshold, and between the L_2 and L_1 thresholds. For the W/C target, the energies have been selected in the region where we had perceived an unexpected behavior of the alignment parameter of $_{73}$Ta or $_{79}$Au. Table I reproduces the values of the L_1, L_2, and L_3 ionization energies of $_{73}$Ta, $_{74}$W, and $_{79}$Au [29].

The beam current has been evaluated from the sum of the charges collected in the Faraday cup and in the irradiation chamber. Losses due to the counting dead time in the acquisition of the x-ray spectra have been corrected according to Ref. [37].

III. DATA ANALYSIS

A. Fitting procedure to determine the parameters of the peaks

The entire L x-ray energy spectrum, which extends from the $L\ell$ line to the $L\gamma$ multiplet, has been fitted simultaneously to a net spectrum deduced from the raw data by removing pile-up [37], Si K escape [36], and theoretical bremsstrahlung components [38]. This allowed us to determine the parameters for each peak.

The chosen model function is the sum of a Voigt function over a smoothed step for each characteristic x-ray line, superimposed on a second-degree polynomial for the remaining continuous component. The FWHM associated with the Gaussian detector response function is $\sqrt{s_0^2 + \kappa E}$, where κ has been fixed to the value fitted to the peaks in the calibration runs and s_0^2 has been regarded as a free parameter. In turn, the natural widths Γ of the Lorentzian profile in the Voigt function have been taken from Ref. [39].

The fit has been done in a single step, including the peaks of the $L\alpha$, $L\beta$, and $L\gamma$ multiplets as well as the $L\ell$, $L\eta$, Lt, and Ls lines [29]. The Lt and Ls lines, although forbidden in the dipole approximation, are visible in the spectra due to the high counting statistics. Hence, they have been incorporated in the model to improve the description of the continuous component of the spectrum.

The adopted fitting procedure is similar to that in Ref. [31], but here the $L\beta$ group is also included. In short, the L multiplet was described by three blocks of lines. In the first one, the position of the $L\alpha_1$ line is the free parameter while the positions of the $L\ell$, Lt, Ls, $L\alpha_2$, and $L\eta$ lines are fixed relatively to it. In the second block, the position of the $L\beta_1$ line is the adjustable parameter and those of the $L\beta_2$, $L\beta_3$, $L\beta_4$, $L\beta_5$, $L\beta_6$, $L\beta_9$, $L\beta_{10}$, $L\beta_{15}$, and $L\beta_{17}$ lines are fixed with respect to it. In the last one, the position of the $L\gamma_1$ line is the free parameter whereas the positions of the $L\gamma_2$, $L\gamma_3$, $L\gamma_{4,4'}$, $L\gamma_5$, and $L\gamma_6$ lines are fixed relatively to it. The experimental radiative transition energies tabulated in Ref. [29] and the energy calibration of the detection system (see Sec. II) have been used to determine the relative positions.

The areas of the Lt and Ls peaks have been regarded as adjustable parameters in the fit whenever the ratios $A_{Lt}/A_{L\alpha}$ and $A_{Ls}/A_{L\alpha}$ are compatible with the ratios of emission rates given in Ref. [40] within two standard deviations, otherwise they have been fixed according to this publication. The $L\beta_{17}$, $L\beta_{15}$, and $L\gamma_6$ peak areas have been fixed with respect to the $L\beta_{17}/L\beta_1$, $L\beta_{15}/L\alpha_1$, and $L\gamma_6/L\gamma_1$ relative intensity ratios, respectively, assuming the values reported in Ref. [40] for the first one, and in Ref. [41] for the last two, after correcting for the spectrometer FEP efficiency. The remaining peak areas have been free parameters in the fit.

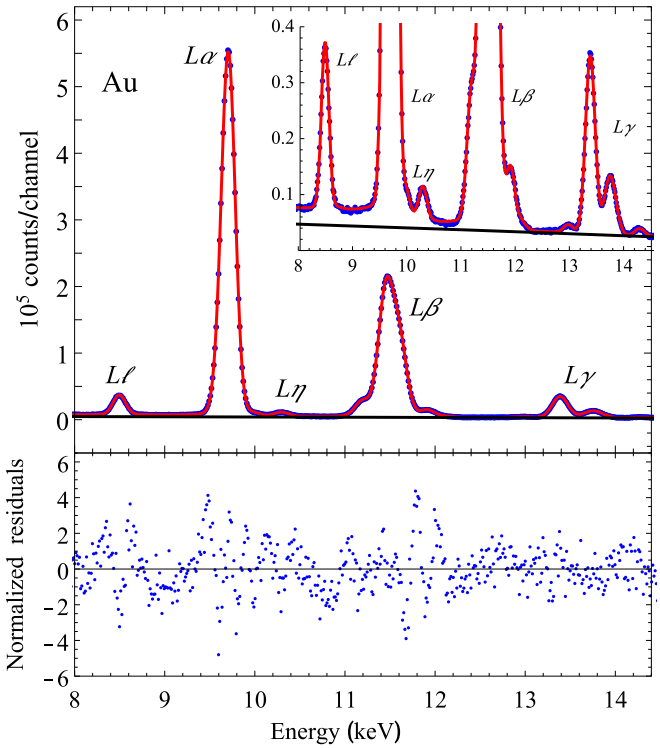

FIG. 4. (a) Experimental spectrum (points) after removal of the pile-up, Si K escape, and theoretical bremsstrahlung distributions, and model function (solid curve) calculated with the fitted parameters for the Au L multiplet, at a detection angle of 31.1°, with 30.62(15) keV electrons. (b) Standardized residuals.

Figure 4 displays the experimental energy spectrum after removal of the pile-up, Si K escape, and theoretical bremsstrahlung distributions for the spectrum acquired at 31.1° while irradiating the Au/C target with a 30.62(15) keV electron beam. The curve calculated with the fitted parameters is also displayed. The corresponding normalized residues are plotted in the lower part.

In the fit used to determine the parameters of the $_{29}$Cu K multiplet, the position of the $K\alpha_1$ line is the adjustable parameter and the $K\alpha_2$ and $K\beta_{1,3}$ ones are fixed with respect to it, also taking as reference the experimental energies from Ref. [29]. All areas of the K peaks have been treated as free parameters in the fit.

The energies and uncertainties of the incident electron beam have been estimated by fitting the tip of the bremsstrahlung spectra as described in Ref. [38]. In this procedure, the detector response function (a Gaussian), taking into account its FEP efficiency curve, is convolved with the bremsstrahlung spectrum calculated according to Refs. [42,43]. The adjustable parameters are the average and width of the electron-beam energy distribution and the bremsstrahlung yield, which have been fitted to the experimental bremsstrahlung spectrum in the tip region.

B. X-ray angular distribution

In the dipole approximation, the angular distribution of the x rays emitted after the decay of L_3 vacancies produced by an unpolarized particle beam can be written as [3,44]

$$W_i(\theta) = \frac{W_{\mathrm{tot},i}}{4\pi}\,[1 + \alpha_i G q_2 A_{20} P_2(\cos\theta)], \tag{4}$$

where $W_i(\theta)$ is the number of counts of the line i detected at the angle θ, measured relative to the incident beam direction, $W_{\mathrm{tot},i}$ is the average number of counts in the ith line, the product Gq_2 corrects for the effects that attenuate the x-ray angular distribution (see below), P_2 is the second-order Legendre polynomial, and α_i is the anisotropy coefficient of the ith line. In the independent-electron model, α_i is a function of the total angular momenta of the initial j_1 and final j_2 states for a single-vacancy ion [3],

$$\alpha_i \equiv (-1)^{j_1+j_2+1}\sqrt{\frac{3}{2}}\sqrt{2j_1+1}\begin{Bmatrix} 1 & j_1 & j_2 \\ j_1 & 1 & 2 \end{Bmatrix}, \tag{5}$$

where {:::} is a Wigner $6j$ symbol. In this work, $j_1 = 3/2$ whereas $j_2 = 1/2$, $3/2$, and $5/2$ for the $L\ell$, $L\alpha_2$, and $L\alpha_1$ transitions, respectively, and the corresponding anisotropy coefficients are $1/2$, $-2/5$, and $1/10$.

Equation (4) can be rewritten in a more compact form as

$$W_i(\theta) = \mathcal{A}_i + \mathcal{B}_i P_2(\cos\theta) \tag{6}$$

with $\mathcal{A}_i = W_{\mathrm{tot},i}/(4\pi)$ and $\mathcal{B}_i = W_{\mathrm{tot},i}\alpha_i G q_2 A_{20}/(4\pi)$. Since Eq. (6) is linear in the parameters $\mathcal{A}_i$ and $\mathcal{B}_i$, the linear least-squares (LLS) method has been used to estimate the alignment parameter, as explained in the following sections.

TABLE III. Estimates of the product $\alpha_K G q_2 A_{20}$ from the parameters of Eq. (6) fitted to the experimental $_{29}$Cu $A_{K\beta}/A_{K\alpha}$ ratios. The numbers in parentheses are the standard deviations in units of the least significant digit.

Energy (keV)	$\alpha_K G q_2 A_{20}$
11.51(6)	0.0008(10)
58.28(3)	0.0001(6)
100.60(3)	0.0002(6)

C. Anisotropy of the experimental setup

The angular dependence of the ratio of peak areas $A_{K\beta}/A_{K\alpha}$, corrected for their FEP efficiencies, has been analyzed for the Cu/C target. The parameters $\mathcal{A}_i$ and $\mathcal{B}_i$ in Eq. (6), for $i = K$, have been fitted to the experimental ratios $A_{K\beta}/A_{K\alpha}$ measured with the three detectors. Figure 5 presents these ratios as well as the curves calculated with the fitted parameters for 11.51, 58.28, and 100.60 keV runs. Table III gives the estimates and uncertainties for the product $\alpha_K G q_2 A_{20}$. After verifying that the Cu K x rays are emitted isotropically, they have been instrumental in ensuring the isotropy of the whole arrangement (beam, target, and detectors) for each irradiation energy.

D. Estimate of the product $\alpha_i G q_2 A_{20}$

A two-step LLS procedure that takes advantage simultaneously of the experimental intensities of the $L\ell$, $L\alpha_1$, and $L\alpha_2$ lines was implemented to estimate the product $\alpha_i G q_2 A_{20}$. In both stages, the estimates of the parameters and their

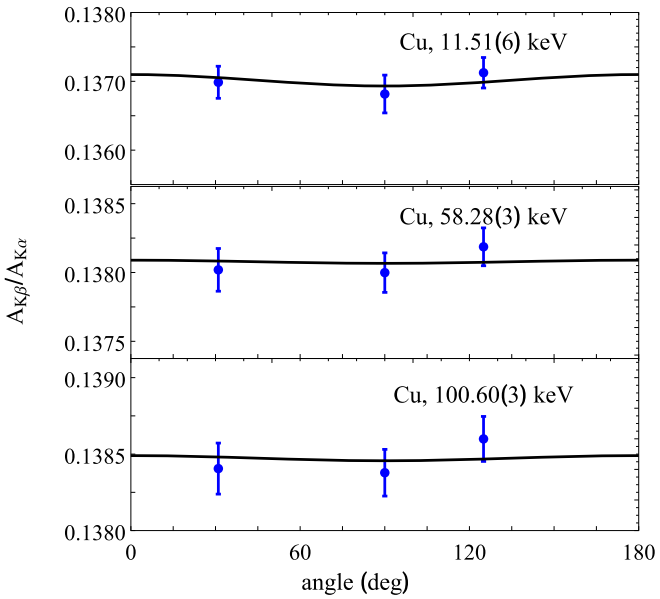

FIG. 5. Experimental ratios $A_{K\beta}/A_{K\alpha}$, corrected for their respective FEP efficiencies (points with uncertainty bars), and corresponding curves calculated from Eq. (6) with the fitted parameters, for the Cu/C target at the indicated energies.

covariance matrix have been obtained by means of the classical expressions [45]

$$\hat{\mathbf{p}} = \left(\mathbb{X}^{\mathrm{T}}\,\mathbb{V}_{\mathbf{y}}^{-1}\,\mathbb{X}\right)^{-1}\mathbb{X}^{\mathrm{T}}\,\mathbb{V}_{\mathbf{y}}^{-1}\,\mathbf{y} \tag{7}$$

and

$$\mathbb{V}_{\hat{\mathbf{p}}} = \left(\mathbb{X}^{\mathrm{T}}\,\mathbb{V}_{\mathbf{y}}^{-1}\,\mathbb{X}\right)^{-1}, \tag{8}$$

where $\hat{\mathbf{p}}$ and $\mathbf{y}$ are the vectors that contain the estimated parameters and the experimental data, respectively, $\mathbb{X}$ is the design matrix, and $\mathbb{V}_{\mathbf{y}}$ and $\mathbb{V}_{\hat{\mathbf{p}}}$ are the covariance matrices of $\mathbf{y}$ and $\hat{\mathbf{p}}$, respectively.

a. First step. We have evaluated the photon yield ratios

$$w_i(\theta) = \frac{A_i}{A_{\mathrm{ref}}}\,\frac{Q_{\mathrm{ref}}}{Q}\,\frac{\varepsilon_{\mathrm{abs}}(E_{\mathrm{ref}})}{\varepsilon_{\mathrm{abs}}(E_i)}\,\frac{1-\phi_{\mathrm{ref}}}{1-\phi}\,\frac{\nu_{\mathrm{ref}}}{\nu_i}, \tag{9}$$

where the subscript i indicates the $L\ell$, $L\alpha_1$, and $L\alpha_2$ lines and the subscript "ref" denotes the $_{29}$Cu $K\alpha$ doublet, A is the area of the fitted Voigt function, Q is the charge incident on the target during the detector acquisition time, $\varepsilon_{\mathrm{abs}}$ is the product of the photon flux transmission and the intrinsic efficiency, as defined in Sec. II, ϕ is the fraction of dead time in the measurement, and ν is the fraction of photons transmitted through the target. All these quantities are evaluated for each SDD because they depend on θ [46]. The ratio of the x-ray yields in Eq. (9) avoids the dependence of the FEP efficiency on the solid angle, thus correcting for fluctuation in the experimental setup, in particular those arising from the small variations of the impact point and focus of the beam; these changes have been smaller than 0.5% in all the runs for the three detectors.

The ratios of efficiencies $\varepsilon_{\mathrm{abs}}(E_{\mathrm{ref}})/\varepsilon_{\mathrm{abs}}(E_i)$ occurring in Eq. (9) are close to one for the lines of the three elements. They have been determined with a precision $\sim 0.04\%$ in a separate experiment performed with the $K\alpha_1$ x-ray lines of Cu and Pd, as described in Sec. II C. The uncertainty of $(1-\phi_{\mathrm{ref}})/(1-\phi)$ was estimated to be less than 0.05% using the methodology of Ref. [37]. The factor ν_{ref}/ν_i corrects for the self-attenuation of the photons in the targets. In the case of the $L\ell$ line, which has the lowest energy of the L multiplet, the values are in the range (0.9999,1.0014) with an uncertainty that could be disregarded compared to the other factors. The uncertainty in the charge Q is less than 0.3% in all irradiations, and the covariances between the values at the three angles are big because the counting dead time fractions are similar. Consequently, the ratios Q_{ref}/Q at the three angles are highly correlated and contributed negligibly to the standard deviations of the parameters to be fitted.

Owing to the isotropy of the Cu K lines, from Eq. (6) it follows that, for each line i, it is possible to write

$$w_i(\theta) = a_i + b_i P_2(\cos\theta) \tag{10}$$

with $a_i = CW_{\mathrm{tot},i}/(4\pi)$, $b_i = CW_{\mathrm{tot},i}\,\alpha_i G q_2 A_{20}/(4\pi)$, and C a constant that changes only with the irradiation energy.

In the first step, the parameters a_i and b_i of the $L\ell$, $L\alpha_1$, and $L\alpha_2$ lines have been fitted simultaneously to the experimental values of $w_i(\theta)$ by an LLS procedure. The vector of experimental data $\mathbf{w}$ is constructed from the $w_{L\ell}$, $w_{L\alpha_1}$, and $w_{L\alpha_2}$ values [see Eq. (9)], the design matrix $\mathbb{X}_1$ is created according to Eq. (10), and the covariance matrix $\mathbb{V}_{\mathbf{w}}$ is calculated from Eq. (9). The estimates of the parameters a_i and b_i for each of the three lines, $\hat{\mathbf{p}}_1$, together with the covariance matrix of the estimated parameters, $\mathbb{V}_{\hat{\mathbf{p}}_1}$, have been determined employing Eqs. (7) and (8), respectively.

b. Second step. The vector of the parameters $\hat{\mathbf{p}}_1$ is used to estimate the product Gq_2A_{20}, by taking into account that

$$\frac{b_i}{a_i} = \alpha_i G q_2 A_{20}. \tag{11}$$

Fitting the product Gq_2A_{20} to the ratios $\hat{b}_i/\hat{a}_i$ also involves an LLS procedure. At this stage, the new matrices are

$$\mathbf{y}_2 = \begin{pmatrix} a_{L\ell} \\ b_{L\ell}/a_{L\ell} \\ a_{L\alpha_1} \\ b_{L\alpha_1}/a_{L\alpha_1} \\ a_{L\alpha_2} \\ b_{L\alpha_2}/a_{L\alpha_2} \end{pmatrix}, \quad \mathbb{V}_{\mathbf{y}_2} = \mathbb{D}\,\mathbb{V}_{\mathbf{p}_1}\mathbb{D}^{\mathrm{T}},$$

$$\mathbb{X}_2 = \begin{pmatrix} 1 & 0 & 0 & 0 \\ 0 & 0 & 0 & \alpha_{L\ell} \\ 0 & 1 & 0 & 0 \\ 0 & 0 & 0 & \alpha_{L\alpha_1} \\ 0 & 0 & 1 & 0 \\ 0 & 0 & 0 & \alpha_{L\alpha_2} \end{pmatrix}, \quad \mathbf{p}_2 = \begin{pmatrix} a_{L\ell} \\ a_{L\alpha_1} \\ a_{L\alpha_2} \\ Gq_2A_{20} \end{pmatrix} \tag{12}$$

with $\mathbf{y}_2$ the experimental data and $\mathbb{V}_{\mathbf{y}_2}$ its covariance matrix, $\mathbb{D}$ the matrix that contains the derivatives of each of the six terms of $\mathbf{y}_2$ with respect to the elements of the vector $\hat{\mathbf{p}}_1$, $\mathbb{X}_2$ the design matrix, and $\mathbf{p}_2$ the vector with the list of parameters to be estimated.

The estimates of the $\hat{\mathbf{p}}_2$ vector and its covariance matrix $\mathbb{V}_{\hat{\mathbf{p}}_2}$ are found by using Eqs. (7) and (8), now with the new matrices presented above.

With the proposed methodology, it is possible to estimate the product Gq_2A_{20} from the $L\ell$, $L\alpha_1$, and $L\alpha_2$ lines

simultaneously, incorporating in a single procedure the $L\ell$ line, which has a large anisotropy but a small intensity, and the $L\alpha_1$ line, which has less anisotropy but the largest intensity.

E. Attenuation factors G and q_2

A vacancy in an L_3 subshell may have been generated by a direct ionization, by a Coster-Kronig transition from L_1 and L_2 subshells, or by a vacancy transfer from the K to the L shells. However, only vacancies in L_3 that are generated by direct ionization will contribute to the emission anisotropy. The fraction of vacancies created by direct ionization of the L_3 subshell is equal to the ratio of the ionization cross section of the L_3 subshell, σ_{L_3}, and the L_3 vacancy-production cross sections, $\sigma^{\rm h}_{L_3}$,

$$G = \frac{\sigma_{L_3}}{\sigma^{\rm h}_{L_3}} \leqslant 1. \tag{13}$$

This factor has been evaluated using ionization cross sections calculated in the distorted-wave Born approximation [47] and Coster-Kronig coefficients extracted from Refs. [48] ($_{73}$Ta, $_{74}$W) and [49] ($_{79}$Au). The ensuing values are $0.8 \lesssim G \leqslant 1$, with an uncertainty below 3%, except when only the L_3 subshell is ionized and $G \equiv 1$ because Coster-Kronig transitions are no longer possible.

In turn, q_2 corrects for the angular deflections of the incident electrons inside the target immediately before the ionization. It can be demonstrated that, in general, each multipole component of the x-ray angular distribution does not change shape but just attenuates when the angular distributions of both the ionizing electron and the emitted x ray are azimuthally symmetric (see Ref. [44], Secs. 9.2–9.4), being the attenuation factor different for each multipole. Here, we have applied this result to the measurements in this work and derive the appropriate formula for q_2, but first we describe how the probability density function (PDF) for the direction of the motion of the ionizing electron has been evaluated. We simulated electron trajectories through the target considering only elastic collisions, with differential cross sections from Ref. [50]. A fraction of about one-thousandth of the electron-atom elastic interactions was sampled as ionization events, with a probability of ionization proportional to the path length from the last collision. The number n of elastic collisions before ionizing an atom has been tallied and gives the corresponding probabilities p_n, therefore p_0 is the fraction of the beam that does not interact with the target atoms and $\sum_{n=0}^{\infty} p_n = 1$. The electron angular deflections θ' after n elastic collisions have also been tallied and normalized to generate the PDFs $f_n(\theta')$, i.e., $\int f_n(\theta')d\Omega' = 1$ where $d\Omega'$ is the solid angle differential. The weighted average of these angular distributions yields the PDF of the direction of motion of the ionizing electron $\mathcal{F}(\theta')$:

$$\mathcal{F}(\theta') = p_0\delta(\theta') + \mathcal{F}_{n\geqslant 1}(\theta') \tag{14}$$

with $\int \delta(\theta')d\Omega' = 1$, and

$$\mathcal{F}_{n\geqslant 1}(\theta') = \sum_{n=1}^{\infty} p_n f_n(\theta'), \tag{15}$$

hence $\int \mathcal{F}(\theta')d\Omega' = 1$ and $\int \mathcal{F}_{n\geqslant 1}(\theta')d\Omega' = 1 - p_0$. We do not include the ϕ' coordinate among the parameters of the distribution functions to stress their azimuthal symmetry. To assess this simulation procedure we have calculated the integral of the angular distribution of the electron beam that emerges from the target in the θ interval $(0^\circ, 12.0^\circ)$, which is the aperture of the Faraday cup [30]. These values agree well with the fractions of charge collected by the Faraday cup in all runs; the details may be consulted in Ref. [51].

The proof that multipole components of the angular distribution function do not change shape has been adapted from the method used in γ-γ angular correlation by Rose [52] and tailored to the conditions in this experiment, noting that $\mathcal{F}(\theta')$ plays the role of the photon detection efficiency of the detector placed at $\theta = 0$ in that article.

In the dipole approximation, the angular distribution of the emitted x rays when there is no elastic electron scattering inside the target takes the form

$$\mathcal{W}(\Theta) \propto 1 + \alpha G A_{20} P_2(\cos\Theta) \tag{16}$$

with Θ the angle between the direction of the emitted photon and the electron beam within the target. Owing to the very small solid angle subtended by the detectors, $\Omega = 1.7 \times 10^{-4}$ sr, only photons emitted toward their angular position (θ, ϕ) measured relative to the incident beam direction, can be detected; this θ is the same angle appearing in Eq. (4).

Accounting for the electron dispersion in the target, the angular distribution of the x rays will be given by the convolution of $\mathcal{W}(\Theta)$ from Eq. (16) with the angular PDF $\mathcal{F}(\theta')$:

$$W(\theta, \phi) = \int \mathcal{W}(\Theta)\mathcal{F}(\theta')d\Omega' \tag{17}$$

and $\Theta = \Theta(\theta', \phi', \theta, \phi)$. Now we resort to the addition theorem

$$P_2(\cos\Theta) = P_2(\cos\theta')P_2(\cos\theta) + \text{terms in } \cos(\phi' - \phi) \text{ and } \cos(2(\phi' - \phi)). \tag{18}$$

Inserting Eqs. (14), (16), and (18) into Eq. (17) and integrating over $d\phi'$ we get

$$W(\theta, \phi) = W(\theta) \propto 1 + \alpha G\left[p_0 + 2\pi \int_0^{\pi} P_2(\cos\theta')\,\mathcal{F}_{n\geqslant 1}(\theta')\sin\theta' d\theta'\right] \times A_{20}P_2(\cos\theta) \tag{19}$$

since the terms with $\cos(\phi' - \phi)$ and $\cos[2(\phi' - \phi)]$ vanish. Defining

$$q_2 \equiv p_0 + 2\pi \int_0^{\pi} \mathcal{F}_{n\geqslant 1}(\theta')P_2(\cos\theta')\sin\theta' d\theta' \tag{20}$$

we arrive at Eq. (4) for the angular distribution of the emitted x rays in the dipole approximation. Equation (19) proves that the angular spreading of the electrons within the target merely changes A_{20} by a multiplicative factor q_2 and that the x-ray angular distribution continues to be described by the Legendre polynomials P_0 and P_2, and it also reveals that the azimuthal position of the detector is irrelevant.

Note that tilting the target with respect to the beam direction, as has been done in this work, breaks the azimuthal

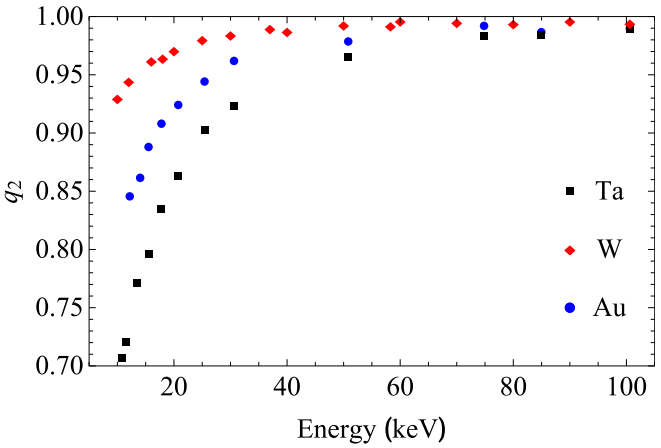

FIG. 6. Dependence of the attenuation parameter of the x-ray angular distribution by electron angular spreading in the $_{73}$Ta, $_{74}$W, and $_{79}$Au targets, with the energy of the incident electron. The thicknesses for each target are given in Sec. II A.

symmetry. However, in the same simulations that furnished the angular distributions of the ionizing electrons, the angular deflections ϕ' have also been tallied and it has been verified that the PDF of ϕ' is compatible with a uniform distribution in $(0, 2\pi)$, which we attribute to the small number of elastic collisions in the thin targets used.

The numerical evaluation of Eq. (20) with the simulated $\mathcal{F}_{n\geqslant 1}(\theta')$ PDFs has yielded $q_2 > 0.7$ for all targets and energies in this experiment, deviating from unity by less than 5% above ∼50 keV, with an uncertainty that decreases from 0.06 to 0.002 as the energy of the incident electron beam increases from 10 to 100 keV [51]. Figure 6 depicts the q_2 values as a function of electron energy for $_{73}$Ta, $_{74}$W, and $_{79}$Au.

IV. THEORY

In order to compare the measured alignment parameter with the theoretical prediction, A_{20} has been calculated in the nonrelativistic plane-wave Born approximation (PWBA) as described in Ref. [3]. The alignment parameter A_{20} is defined equivalently as

$$A_{20} \equiv \frac{\rho_{20}(j_1 j_1)}{\rho_{00}(j_1 j_1)}, \tag{21}$$

where ρ_{k0} is the statistical tensor of order k and component 0. Applying the definition of the statistical tensors expressed in terms of the elements of the density matrix of the system, Eq. (1) in Ref. [3], it is possible to prove that for a set of ions with a vacancy in the L_3 subshell Eq. (21) corresponds to the relative difference of the ionization cross sections presented in Eq. (1).

The statistical tensors ρ_{k0} in Eq. (21) can be expressed as

$$\rho_{k0}(j, j) = \frac{8\pi e^4}{m_e v^2} \int_0^{E-E_{\rm ion}} d\epsilon \int_{q_-(\epsilon)}^{q_+(\epsilon)} F_k(q, \epsilon) \frac{dq}{q^3}, \tag{22}$$

where v is the velocity of the incident electron, q is the momentum transfer, ϵ is the kinetic energy of the ejected electron, and $E_{\rm ion}$ is the ionization energy of the considered (sub)shell; m_e is the electron rest mass and e is the elementary charge. The factor $F_k(q, \epsilon)$ is given by [3,53]

$$F_k(q, \epsilon) = C(k, \ell, j) \left[\sum_{\ell'} \sum_{\lambda_1, \lambda_2} B(k, \ell, \ell', \lambda_1, \lambda_2) R^{\lambda_1}_{\epsilon\ell', n\ell}(q) R^{\lambda_2}_{\epsilon\ell', n\ell}(q) \right] P_k(\cos\theta_r) \tag{23}$$

with the coefficients

$$C(k, \ell, j) = (-1)^{j+(1/2)} (2j+1)(2\ell+1) \begin{Bmatrix} \ell & k & \ell \\ j & \frac{1}{2} & j \end{Bmatrix} \tag{24}$$

and

$$B(k, \ell, \ell', \lambda_1, \lambda_2) = \sqrt{2k+1}\,(-1)^{\ell'+(1/2)(\lambda_1-\lambda_2)}(2\ell'+1)(2\lambda_1+1)(2\lambda_2+1) \times \begin{pmatrix} \lambda_1 & \lambda_2 & k \\ 0 & 0 & 0 \end{pmatrix} \begin{pmatrix} \ell & \lambda_1 & \ell' \\ 0 & 0 & 0 \end{pmatrix} \begin{pmatrix} \ell & \lambda_2 & \ell' \\ 0 & 0 & 0 \end{pmatrix} \begin{pmatrix} \ell & k & \ell \\ \lambda_1 & \ell' & \lambda_2 \end{pmatrix}, \tag{25}$$

where n, ℓ, j are the quantum numbers of the electron in the orbital where the vacancy is produced, ℓ' is the angular momentum of the ejected electron, θ_r is the angle between the momentum transfer vector and the direction of the incident beam, P_k are Legendre polynomials, and (:::) and {:::} are Wigner $3j$ and $6j$ symbols, respectively.

The radial integrals $R^{\lambda}_{\epsilon\ell', n\ell}$ are

$$R^{\lambda}_{\epsilon\ell', n\ell}(q) \equiv \int_0^{\infty} dr\, P_{\epsilon\ell'}(r) j_\lambda(qr/\hbar) P_{n\ell}(r) \tag{26}$$

with j_λ the spherical Bessel function of order λ, $P_{n\ell}$ the reduced radial wave function of the bound state, and $P_{\epsilon\ell'}$ the angular momentum component ℓ' of the ejected electron wave function with kinetic energy ϵ, normalized on the energy scale. The integration limits in Eq. (22) for the integral over q can be deduced from the collision kinematics,

$$q_\pm = \sqrt{2m_e}\left[\sqrt{E} \pm \sqrt{E - (E_{\rm ion} + \epsilon)}\right]. \tag{27}$$

The target atoms have been described with self-consistent Dirac-Hartree-Slater potentials [54], and the radial wave functions of the bound and free states have been computed with the RADIAL subroutine package [54]. $E_{\rm ion}$ (= E_{L_3} in the present case) was extracted from Ref. [29] (see Table I). Partial waves have been added to the sum in ℓ' of Eq. (23) until the relative

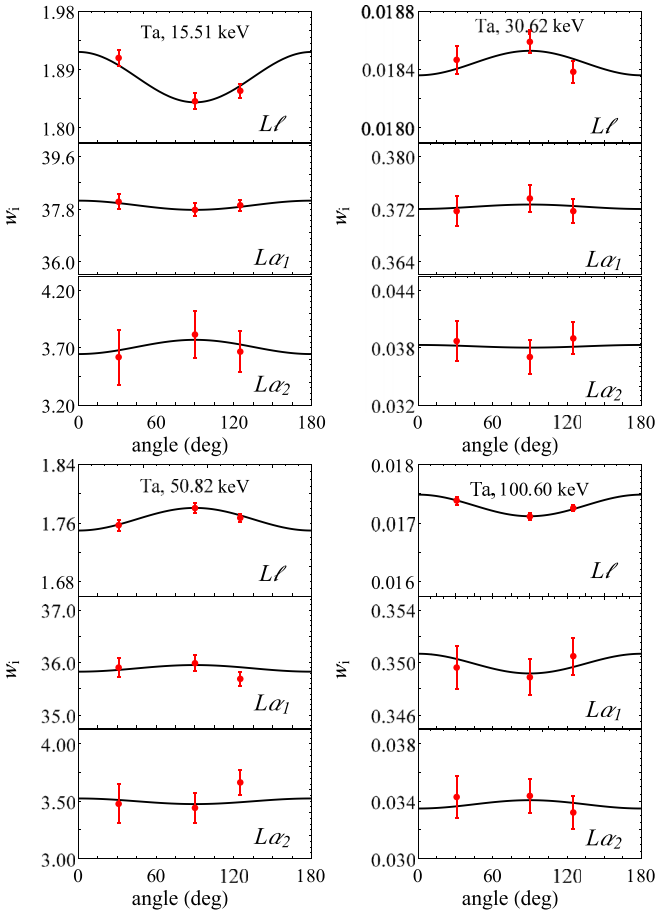

FIG. 7. Angular dependence, $w_i(\theta)$, in the emission of the $i = L\ell$, $L\alpha_1$, and $L\alpha_2$ characteristic x rays of $_{73}$Ta for electron energies of 15.51(4), 30.62(15), 50.82(5), and 100.60(4) keV. The symbols with uncertainty bars (one standard deviation) are our experimental values. The solid curves are the predictions of Eq. (10) calculated with fitted parameters to the experimental values. Note that at 30.62(15) keV the $L\ell$, $L\alpha_1$, and $L\alpha_2$ x rays are emitted almost isotropically.

difference between the values for the alignment parameter calculated in successive iterations was smaller than 10^{-4}, evaluated individually for each combination of energy and atom. The calculations requires the inclusion of 3 to 20 partial waves to converge as the electron energy grows from $1.02E_{L_3}$ to $10.2E_{L_3}$.

V. RESULTS

Figures 7–9 display the $L\ell$, $L\alpha_1$, and $L\alpha_2$ x-ray angular distributions for various energies of the incident electron beam. The interpretation of these figures needs attention because the plotted experimental data are the ratios $w_i(\theta)$, Eq. (9), which are statistically correlated. In addition, as the scales in the graphs are not chosen with the same relative amplitude, for a proper comparison of the $L\ell$, $L\alpha_1$, and $L\alpha_2$ anisotropies it is necessary to read the y-axis scales carefully. The angular distributions for all energies and targets (totaling 27 situations) along with the chi squares for the fitted values are collected in Ref. [55].

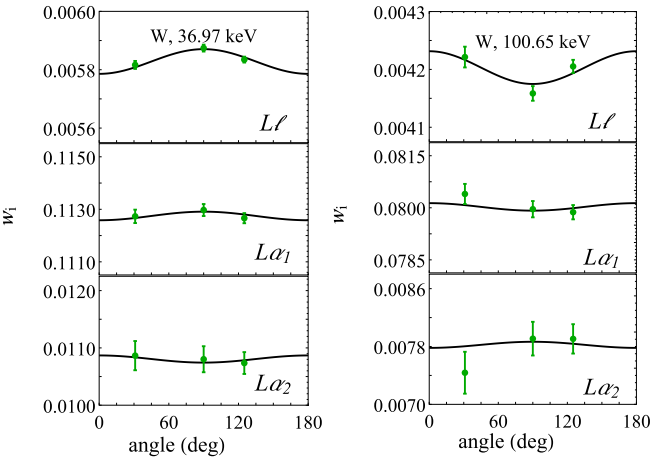

FIG. 8. Same as Fig. 7 but for the $_{74}$W target irradiated with 36.97(8) and 100.65(7) keV electrons.

The alignment parameters A_{20} estimated for $_{73}$Ta, $_{74}$W, and $_{79}$Au are presented in Tables IV, V, and VI, respectively, together with the theoretical PWBA values, Eqs. (21) and (22), calculated employing Dirac-Hartree-Slater potentials.

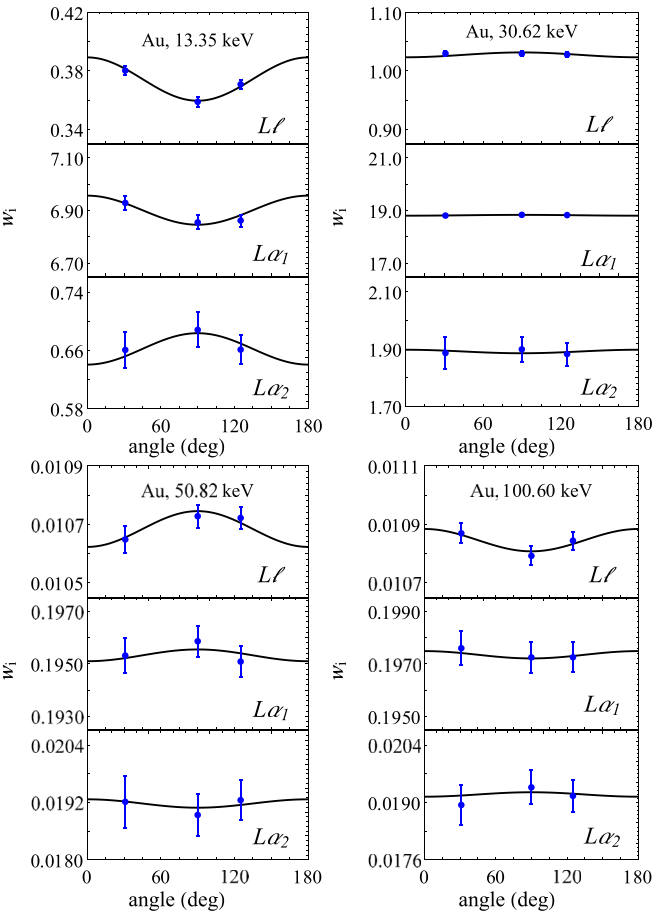

FIG. 9. Same as Fig. 7 but for the $_{79}$Au target irradiated with 13.35(9), 30.62(15), 50.82(7), and 100.60(4) keV electrons. Note that at 30.62(15) keV the $L\ell$, $L\alpha_1$, and $L\alpha_2$ x rays are emitted almost isotropically.

TABLE IV. Alignment parameter of $_{73}$Ta for the electron energies of the present experiment. $A_{20}^{\rm raw}$ denotes the fitted value for the product Gq_2A_{20}, $A_{20}^{\rm expt}$ the corrected value for the Coster-Kronig transitions and the opening of the electron beam inside the target, and $A_{20}^{\rm theor}$ the theoretical value calculated in the PWBA with Dirac-Hartree-Slater atomic potentials. The numbers in parentheses are the standard deviations in units of the least significant digit.

Energy (keV)	$A_{20}^{\rm raw}$	$A_{20}^{\rm expt}$	$A_{20}^{\rm theor}$
10.75(9)	0.132(21)	0.197(34)	0.108
11.51(6)	0.077(13)	0.110(20)	0.095
13.46(9)	0.057(7)	0.078(11)	0.066
15.51(4)	0.057(13)	0.076(18)	0.045
17.79(7)	0.025(7)	0.032(9)	0.027
20.76(9)	0.014(12)	0.016(16)	0.010
25.41(15)	0.006(6)	0.006(7)	−0.006
30.62(9)	−0.012(10)	−0.015(12)	−0.018
50.82(5)	−0.021(7)	−0.027(8)	−0.030
74.83(6)	0.003(8)	0.002(9)	−0.028
84.96(5)	0.015(7)	0.014(8)	−0.026
100.60(4)	0.031(6)	0.034(7)	−0.022

$A_{20}^{\rm raw}$ corresponds to the experimental result without the corrections for the Coster-Kronig transitions and the electron beam scattering within the target (Gq_2A_{20} from the fit). On the other hand, $A_{20}^{\rm expt}$ is the corrected alignment parameter. The calculated values of A_{20} are represented in Fig. 10 for the three elements and all the energies of the experiment.

The vector $\hat{\mathbf{p}}$ with the estimates of the parameters, Eq. (7), is the unique solution of the LLS procedure. It may be worth remembering that experimental points displaced from the fitted curve must happen with a frequency dictated by the residue PDF, and many angular distributions have been measured, therefore many apparent differences can be spotted in the complete set of graphs [55]. However, each dataset has passed the chi-square test. As our procedure includes the $L\ell$, $L\alpha_1$, and $L\alpha_2$ lines simultaneously, there are nine experimental values and four parameters to be fitted for each energy, amounting to five degrees of freedom (d.f.). Evaluating the sum of all chi squares for the $_{73}$Ta and $_{79}$Au data, which have 60 d.f., we found 82 and 67 for the absolute chi-squares, respectively. The probabilities of these chi squares being exceeded are 5% and 23%, respectively. For the $_{74}$W data there are 15 d.f. and the absolute chi square is 25, corresponding to a probability of being exceeded equal to 5%. Then, the sum of all chi squares cannot be rejected, validating the standard deviations quoted in Tables IV–VI and plotted in Fig. 10 as uncertainty bars.

Figure 11 shows the variation of A_{20} with E/E_{L_3}, comparing our estimates of the alignment parameter with those reported in the literature from the analysis of the x rays emitted when the ionization occurs by electron impact, Fig. 1.

TABLE V. Same as Table IV but for $_{74}$W.

Energy (keV)	$A_{20}^{\rm raw}$	$A_{20}^{\rm expt}$	$A_{20}^{\rm theor}$
36.97(8)	−0.019(5)	−0.022(6)	−0.024
58.28(3)	−0.011(7)	−0.013(8)	−0.031
100.65(7)	0.018(8)	0.021(9)	−0.022

TABLE VI. Same as Table IV but for $_{79}$Au.

Energy (keV)	$A_{20}^{\rm raw}$	$A_{20}^{\rm expt}$	$A_{20}^{\rm theor}$
12.19(9)	0.22(5)	0.26(6)	0.121
13.35(9)	0.107(15)	0.123(17)	0.103
14.03(9)	0.081(16)	0.095(19)	0.093
15.51(9)	0.076(19)	0.092(23)	0.075
17.79(11)	0.039(9)	0.049(11)	0.052
20.76(8)	0.029(13)	0.036(16)	0.031
25.41(9)	0.004(6)	0.005(7)	0.009
30.62(15)	−0.011(8)	−0.014(10)	−0.007
50.82(7)	−0.015(8)	−0.019(10)	−0.029
74.83(7)	−0.015(7)	−0.019(9)	−0.030
84.96(6)	−0.012(7)	−0.015(9)	−0.029
100.60(4)	0.009(6)	0.011(7)	−0.026

VI. DISCUSSION

From Figs. 7–10 it is possible to conclude that the $L\ell$, $L\alpha_1$, and $L\alpha_2$ x rays are not emitted isotropically for energies close to the L_3 ionization threshold. When the beam energy is near $2.5E_{L_3}$ the emission of the three investigated lines

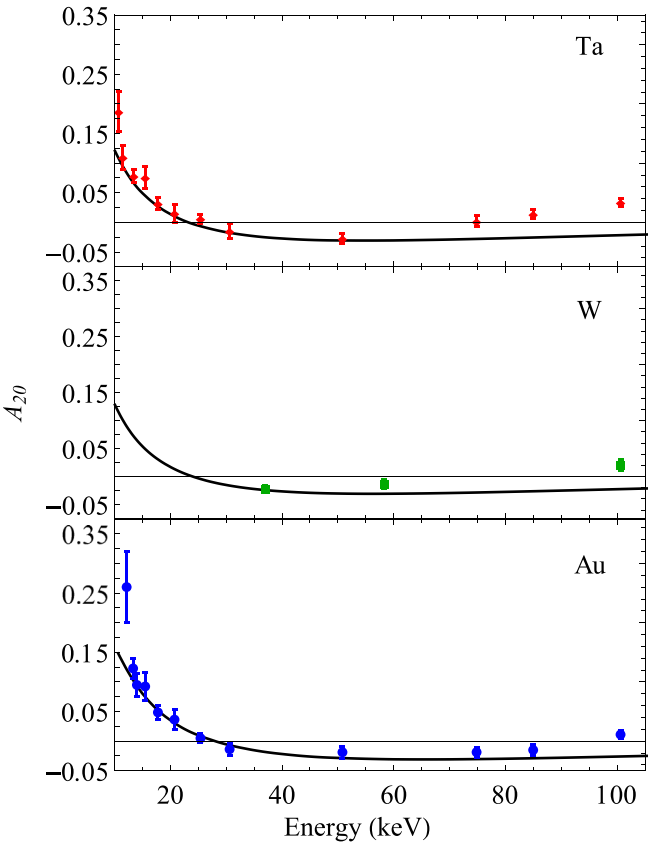

FIG. 10. Alignment parameter A_{20} of $_{73}$Ta, $_{74}$W, and $_{79}$Au as a function of electron energy. The symbols with uncertainty bars (one standard deviation) are the present experimental values. The solid curves are the predictions of the PWBA.

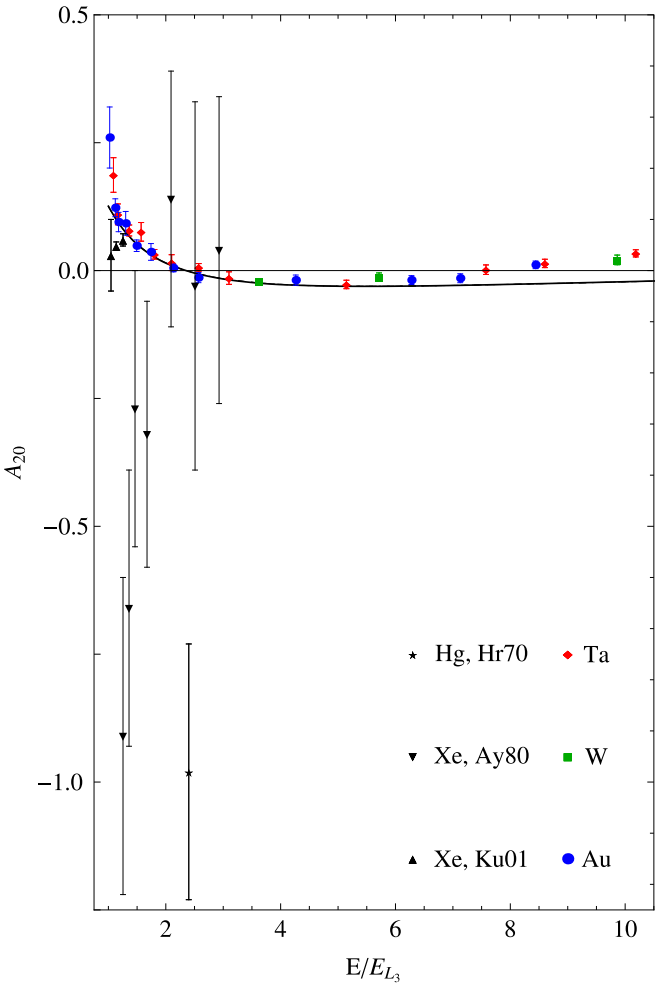

FIG. 11. Alignment parameter A_{20} of $_{73}$Ta, $_{74}$W, and $_{79}$Au as a function of electron energy divided by the L_3 threshold energy. The red diamonds, green squares, and blue circles are the experimental values, and the uncertainty bars correspond to one standard deviation. The black symbols (stars, up triangles, and down triangles) are the same as those that appear in Fig. 1; Hg [10], Xe [12], and Xe [13]. The solid curve gives the calculated values for the three elements which, although not identical, differ by amounts that are not visible in this scale.

becomes practically isotropic; around (3–7)E_{L_3} a nonisotropic emission is found again but with an opposite sign to that seen initially, and above $8E_{L_3}$ there is a second inversion in the sign of the anisotropy. These results also confirm the theoretical expectation that the anisotropies of the $L\alpha_1$ and $L\alpha_2$ x rays have opposite signs.

The experimental values of A_{20}, Fig. 10, exhibit the evolution of the alignment parameter with the electron energy in a wide energy interval beginning near the ionization threshold. Two sign inversions can be seen, which is unexpected both considering the theoretical calculations and the previous experiments, whose results had very large uncertainty bars that precluded their observation. The experimental and calculated values of A_{20} agree for incident electron energies below ∼60 keV, i.e., up to $\sim 6E_{L_3}$. Above this energy, the results of the experiment show, for the three elements, a second sign inversion that is not predicted by the theory outlined in Sec. IV. This effect cannot be related to the indirect production of a vacancy in the L_3 subshell via ionization of the K shell and subsequent transfer of the vacancy to the L_3 subshell; in fact, the fraction of the total number of L_3 vacancies that originate in K-shell ionization is negligible because the K ionization cross section is two orders of magnitude smaller than that of the L_3 subshell. The explanation for this discrepancy probably lies in the use of a nonrelativistic formalism as well as in the neglect of Coulomb and exchange effects.

The dependence of A_{20} on E/E_{L_3} is the same, within uncertainties, for the three studied elements (see Fig. 11). A similar behavior was reported by Jitschin *et al.* [23] for the ionization by proton impact but, at variance with our work, their results follow the trend of the theoretical calculations. We point out that, in the ionization by nonrelativistic positive ions, the energy of the ejected electron is not sufficiently high to cause significant relativistic effects, which is not the case for electron-impact ionization of the L subshells of $_{73}$Ta, $_{74}$W, and $_{79}$Au L at energies above several tens of keV.

The effect of the alignment parameter on the measured L subshell ionization cross sections of high-Z elements can be assessed consulting, e.g., Ref. [31]. When the L_3 ionization cross section is deduced from the $L\ell$, $L\alpha_1$, and $L\alpha_2$ x-ray production cross sections, the uncertainty of the measured values should be less than 1% to be affected by atomic alignment with the order of magnitude found here. This follows from the small average anisotropy that results from the sum of the anisotropy coefficients weighted by the intensities of the lines. However, if the L_3 ionization cross section is estimated from just the $L\ell$ yield, the anisotropy needs to be included near the ionization threshold wherever the uncertainties in the cross sections are smaller than 5%, as a consequence of the large values $\alpha_{L\ell} = 1/2$ and $A_{20} \sim 0.1$ near the threshold.

As pointed out by Yamaoka *et al.* [18,19] and Santra *et al.* [21], the use of SDDs to measure the x-ray angular distribution actually introduces an additional difficulty because they cannot resolve completely the $L\alpha_1$ and $L\alpha_2$ lines. However, we have been able to overcome this shortcoming by means of two strategies. The first one has been to fit all lines in the L multiplet, in particular the $L\ell$ line and the $L\alpha$ doublet, in a single fit procedure, which yields not only the estimates of the areas but also their covariances. The second strategy has been to use the areas of the $L\ell$, $L\alpha_1$, and $L\alpha_2$ peaks simultaneously in the procedure to estimate A_{20}, including at this stage their covariances.

The accuracy of the present experimental results could be achieved thanks to the significant improvements made in the experimental setup and analysis procedures, from which relevant characteristics not described in the literature will be highlighted.

If we had not employed the intensity ratio between the x ray of interest and the Cu $K\alpha$ line, only A_{20} values above 0.1 would differ from zero by more than two standard deviations, even if the Cu $K\alpha$ line intensity variation is in the interval (0.995; 1.001), corresponding to changes in the average position of the electron beam spot on the target of less than 0.5 mm.

Below $2E_{L_3}$ it is crucial to determine the photon yield simultaneously at the three angles because changes in the average electron energy as small as 50 eV modify the photon

yields as strongly as the x-ray angular distribution, or even more in the case of the $L\alpha_1$ line, due to the fast growth of the $L\alpha$ x-ray production cross section in this energy region.

The use of thin solid targets with an area of only 0.5 cm^2 and C fiber frames and holders, developed for inner-shell ionization measurements [30], minimized the photon background and reduced the elastic scattering of the electron beam within the target, which influences the measurement of the photon angular distributions and was ignored in earlier publications [14].

Lastly, the use of the $L\ell$, $L\alpha_1$, and $L\alpha_2$ lines in a single procedure to estimate A_{20}, although unimportant below $\sim$20 keV (corresponding to $A_{20} > 0.05$), reduces the standard deviation of the values measured above this energy to roughly one-half of that obtained using exclusively the $L\ell$ line, as had been done in Refs. [13,19]. This is because the increase of bremsstrahlung events in the $L\ell$ peak region is faster than that of the ionization yield, deteriorating the statistical uncertainty in the measured intensity of this relatively weak line.

VII. CONCLUSION

The atomic alignment parameter in the electron-impact ionization of the L_3 subshell has been measured in a wide energy interval. Two inversions in the sign of A_{20} appear between 10 and 100 keV, one of them not predicted by the nonrelativistic PWBA. The alignment parameter of high-Z elements turns out to be nearly independent of Z when plotted as a function of E/E_{L_3}. The calculations disagree quantitatively and qualitatively with the experimental results only for electron energies $\gtrsim$60 keV, suggesting that the adoption of a consistent relativistic formalism might improve the theoretical predictions. This sign inversion is sensitive to the fine details of the ionization process and the wave functions involved, and it will help in recognizing differences in models that cannot be distinguished by measurements of total ionization cross sections. Analyzing our results in conditions similar to those of other researchers that attempted to measure the x-ray emission anisotropy, it has been possible to understand why they were unable to observe conclusively the sign inversion at electron energies $\sim 8E_{L_3}$.

Finally, although the x-ray transitions from L_3 vacancies produced by electron impact do not have an isotropic distribution, the observation of the ensuing angular correlation effects requires very special conditions, unlikely to be found in the usual arrangements. In particular, in the measurement of L-subshell ionization cross sections it will affect the results only if the relative uncertainties approach 1%, which is still far from the current experimental precision.

ACKNOWLEDGMENTS

We thank W. G. P. Engel, A. C. Tromba, and A. D. Santos for preparing the samples, and the technical staffs of the São Paulo Microtron and LAMFI for the operation of the accelerators. This work was funded by the Brazilian agencies FAPESP (Fundação de Amparo à Pesquisa do Estado de São Paulo), Projects No. 2013/24803-5, No. 2015/14530-7, and No. 2016/13116-5, and CNPq (Conselho Nacional de Desenvolvimento Científico e Tecnológico), Grant No. 306331/2016-0. J.M.F.-V. thanks the Universidade de São Paulo for support from a Visiting Professorship and the support from the Spanish Ministerio de Economía y Competitividad (Project No. FIS2014-58849-P).

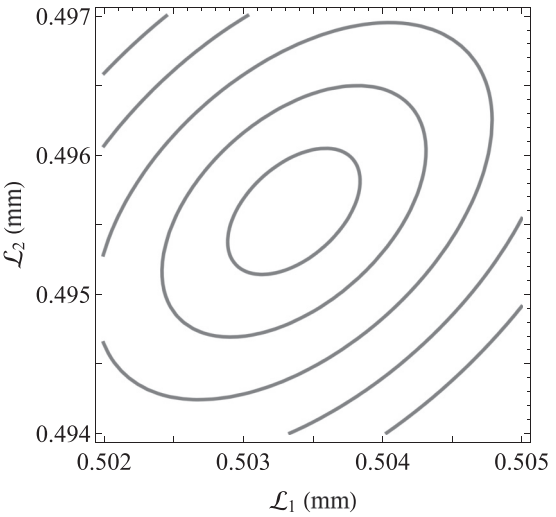

FIG. 12. Cut through the contour surfaces of the merit function $\hat{Q}(\mathcal{L}_1, \mathcal{L}_2, \mathcal{L}_3) + m^2$, with $m = 1, \ldots, 5$, for $\mathcal{L}_3 = 0.4885$ mm, corresponding to the lowest $\hat{Q}$, which is 18.2.

APPENDIX: RELATIVE EFFICIENCY

The model given by Eq. (3) has allowed us to write the merit function for the least-squares fit as

$$\hat{Q}(\mathcal{L}_1, \mathcal{L}_2, \mathcal{L}_3) = \sum_E \sum_{n=1}^{3} \left[\frac{r_{E,n}^{\text{expt}} - \mathcal{C}(E)\, R_{\varepsilon_{\text{abs}}}(\mathcal{L}_n)}{\sigma_{r_{E,n}}} \right]^2, \quad \text{(A1)}$$

where $\sigma_{r_{E,n}}$ is the standard deviation of $r_{E,n}^{\text{expt}}$. The hat over the Q symbol means that $\mathcal{C}(E)$ is the least-squares estimate for each value assigned to $\mathcal{L}_1$, $\mathcal{L}_2$, and $\mathcal{L}_3$ thickness. Each $\varepsilon_{\text{abs}}(\mathcal{L}_n)$ in the efficiency ratio $R_{\varepsilon_{\text{abs}}}(\mathcal{L}_n)$ of Eq. (3) is calculated from the analytical model, as described at the beginning of Sec. II C.

The graph of the merit function given by Eq. (A1) forms a surface whose contours, i.e., cuts at constant $\hat{Q}$ allow one to graphically estimate the thicknesses $\mathcal{L}_1$, $\mathcal{L}_2$, and $\mathcal{L}_3$ that minimized the function. Figure 12 shows the contour lines when a cut is made at $\mathcal{L}_3 = 0.4885$ mm, for $\hat{Q}(\mathcal{L}_1, \mathcal{L}_2, \mathcal{L}_3) + m^2$ with $m = 1, \ldots, 5$. The standard deviation of the thickness estimates has been calculated from Eq. (8), employing the fitted values for thicknesses. The chi square of the fit with 9 d.f. is 18.2, which marginally satisfies the χ^2 test. The thicknesses estimated with this method are in good agreement with those ensuing from the fit of the parameters of the analytical model to the experimental data, and also with that reported in Ref. [35], but with an improvement of one order of magnitude in precision.

[1] A. Bohr, Rev. Mod. Phys. **48**, 365 (1976).
[2] N. Andersen, J. W. Gallagher, and I. V. Hertel, Phys. Rep. **165**, 1 (1988).
[3] E. G. Berezhko and N. M. Kabachnik, J. Phys. B **10**, 2467 (1977).
[4] B. Cleff and W. Mehlhorn, Phys. Lett. A **37**, 3 (1971).
[5] E. Dobelin, W. Sandner, and W. Mehlhorn, Phys. Lett. A **49**, 7 (1974).
[6] W. Sandner and W. Schmitt, J. Phys. B **11**, 1833 (1978).
[7] R. DuBois and M. Rødbro, J. Phys. B **13**, 3739 (1980).
[8] W. Weber, R. Huster, M. Kamm, and W. Mehlhorn, Z. Phys. D **22**, 419 (1991).
[9] W. Mehlhorn, Nucl. Instrum. Methods Phys. Res. B **87**, 227 (1994).
[10] J. Hrdý, A. Henins, and J. A. Bearden, Phys. Rev. A **2**, 1708 (1970).
[11] J. Pálinkás, B. Schlenk, and A. Valek, J. Phys. B **12**, 3273 (1979).
[12] M. Aydinol, R. Hippler, T. McGregor, and H. Kleinpoppen, J. Phys. B **13**, 989 (1980).
[13] H. Küst and W. Mehlhorn, J. Phys. B **34**, 4155 (2001).
[14] G. Sestric, S. Ferguson, I. Wright, and S. Williams, Radiat. Phys. Chem. **102**, 40 (2014).
[15] K. S. Kahlon, N. Singh, R. Mittal, B. S. Sood, and K. L. Allawadhi, Phys. Rev. A **48**, 1701 (1993).
[16] J. K. Sharma and K. L. Allawadhi, J. Phys. B **32**, 2343 (1999).
[17] A. Kumar, M. L. Garg, S. Puri, D. Mehta, and N. Singh, X-Ray Spectrom. **30**, 287 (2001).
[18] H. Yamaoka, M. Oura, K. Takahiro, N. Takeshima, K. Kawatsura, M. Mizumaki, U. Kleiman, N. M. Kabachnik, and T. Mukoyama, Phys. Rev. A **65**, 062713 (2002).
[19] H. Yamaoka, M. Oura, K. Takahiro, T. Morikawa, S. Ito, M. Mizumaki, S. Semenov, N. Cherepkov, N. Kabachnik, and T. Mukoyama, J. Phys. B **36**, 3889 (2003).
[20] H. Yamaoka, M. Oura, K. Takahiro, K. Kawatsuta, S. Ito, M. Mizumaki, H. Oohashi, Y. Ito, and T. Mukoyama, J. Phys. B **39**, 2747 (2006).
[21] S. Santra, D. Mitra, M. Sarkar, and D. Bhattacharya, Phys. Rev. A **75**, 022901 (2007).
[22] T. Kampfer, I. Uschmann, Z. W. Wu, A. Surzhykov, S. Fritzsche, E. Forster, and G. G. Paulus, Phys. Rev. A **93**, 033409 (2016).
[23] W. Jitschin, H. Kleinpoppen, R. Hippler, and H. O. Lutz, J. Phys. B **12**, 4077 (1979).
[24] W. Jitschin, R. Hippler, R. Shanker, H. Kleinpoppen, R. Schuch, and H. O. Lutz, J. Phys. B **16**, 1417 (1983).
[25] T. Papp, J. L. Campbell, and J. A. Maxwell, Phys. Rev. A **48**, 3062 (1993).
[26] O. G. de Lucio and J. Miranda, Nucl. Instrum. Methods Phys. Res. B **248**, 47 (2006).
[27] X. Llovet, C. J. Powell, F. Salvat, and A. Jablonski, J. Phys. Chem. Ref. Data **43**, 013102 (2014).
[28] M. S. Pindzola, J. Phys. B **48**, 015201 (2014).
[29] R. D. Deslattes, E. G. Kessler, Jr., P. Indelicato, L. de Billy, E. Lindroth, and J. Anton, Rev. Mod. Phys. **75**, 35 (2003).
[30] V. R. Vanin, N. L. Maidana, A. Mangiarotti, R. R. Lima, A. A. Malafronte, S. F. Barros, and M. N. Martins, Radiat. Phys. Chem. **154**, 26 (2019).
[31] S. F. Barros, V. R. Vanin, N. L. Maidana, M. N. Martins, J. A. García-Alvarez, O. C. B. Santos, C. L. Rodrigues, M. F. Koskinas, and J. M. Fernández-Varea, J. Phys. B **51**, 025201 (2018).
[32] J. A. García-Alvarez, J. M. Fernández-Varea, V. R. Vanin, and N. L. Maidana, J. Phys. B **51**, 225003 (2018).
[33] O. C. B. Santos, V. R. Vanin, N. L. Maidana, M. N. Martins, M. H. Tabacniks, C. L. Rodrigues, T. F. Silva, A. D. Santos, S. F. Barros, J. A. García-Alvarez, M. F. Koskinas, J. M. Fernández-Varea, and M. S. Pindzola, Phys. Rev. A **100**, 022703 (2019).
[34] T. F. Silva, C. L. Rodrigues, M. Mayer, M. V. Moro, G. F. Trindade, F. R. Aguirre, N. Added, M. A. Rizzutto, and M. H. Tabacniks, Nucl. Instrum. Methods Phys. Res. B **371**, 86 (2016).
[35] S. F. Barros, N. L. Maidana, J. M. Fernández-Varea, and V. R. Vanin, X-Ray Spectrom. **46**, 34 (2017).
[36] S. M. Seltzer, Nucl. Instrum. Methods **188**, 133 (1981).
[37] S. F. Barros, V. R. Vanin, A. A. Malafronte, N. L. Maidana, and M. N. Martins, J. Synchrotron Rad. **25**, 484 (2018).
[38] J. M. Fernández-Varea, V. Jahnke, N. L. Maidana, A. A. Malafronte, and V. R. Vanin, J. Phys. B **47**, 155201 (2014).
[39] M. O. Krause and J. H. Oliver, J. Phys. Chem. Ref. Data **8**, 329 (1979).
[40] J. H. Scofield, At. Data Nucl. Data Tables **14**, 121 (1974).
[41] J. L. Campbell and J. X. Wang, At. Data Nucl. Data Tables **43**, 281 (1989).
[42] S. M. Seltzer and M. J. Berger, At. Data Nucl. Data Tables **35**, 345 (1986).
[43] L. Kissel, C. A. Quarles, and R. H. Pratt, At. Data Nucl. Data Tables **28**, 381 (1983).
[44] A. J. Ferguson, *Angular Correlation Methods in Gamma Ray Spectroscopy* (North Holland, Amsterdam, 1965).
[45] W. T. Eadie, D. Drijard, E. F. James, M. Roos, and B. Sadoulet, *Statistical Methods in Experimental Physics* (North Holland, Amsterdam, 1971).
[46] The dependence of the parameters ν and Q on θ is indirect because each detector is placed at a different angle and has a different dead time that is directly associated with its counting rate.
[47] D. Bote and F. Salvat, Phys. Rev. A **77**, 042701 (2008).
[48] M. O. Krause, J. Phys. Chem. Ref. Data **8**, 307 (1979).
[49] M. Kolbe, P. Hönicke, M. Müller, and B. Beckhoff, Phys. Rev. A **86**, 042512 (2012).
[50] P. M. DeLuca, J. ICRU **7**, 5 (2007).
[51] S. F. Barros, V. R. Vanin, A. Mangiarotti, N. L. Maidana, and J. M. Fernández-Varea (unpublished).
[52] M. E. Rose, Phys. Rev. **91**, 610 (1953).
[53] V. V. Sizov and N. M. Kabachnik, J. Phys. B **13**, 1601 (1980).
[54] F. Salvat and J. M. Fernández-Varea, Comput. Phys. Commun. **240**, 165 (2019).
[55] S. F. Barros, Ph.D. thesis, Universidade de São Paulo, Brazil (in Portuguese), 2018, http://www.teses.usp.br/teses/disponiveis/43/43134/tde-14062018-103044/es.php.